Improving Satellite Estimates of the Fraction of Absorbed Photosynthetically Active Radiation Through Data Integration: Methodology and Validation

Xin Tao🆔, Shunlin Liang🆔, *Fellow, IEEE*, Dongdong Wang🆔, Tao He🆔, and Chengquan Huang

Abstract—The fraction of absorbed photosynthetically active radiation (FAPAR) is a critical input in many climate and ecological models. The accuracy of satellite FAPAR products directly influences estimates of ecosystem productivity and carbon stocks. The targeted accuracy of FAPAR products is 10% or 0.05 for many applications. However, most current FAPAR products do not meet such requirements, and further improvements are still needed. In this paper, a data fusion scheme based on the multiple resolution tree (MRT) approach is developed to integrate multiple satellite FAPAR estimates at site and regional scales. MRT was chosen because of the superior computational efficiency compared with other fusion methods. The fusion scheme removed the bias in FAPAR estimates and resulted in a 15% increase in the R^2 and 3% reduction in the root-mean-square error compared with the average of individual FAPAR estimates. The regional-scale fusion filled in the missing values, and provided spatially consistent FAPAR distributions at different resolutions. Overall, MRT can be used to efficiently and accurately generate spatially and temporally continuous FAPAR data across both site and regional scales.

Index Terms—Data fusion, fraction of absorbed photosynthetically active radiation (FAPAR) integration, Landsat, Moderate Resolution Imaging Spectroradiometer (MODIS), Multi-angle Imaging SpectroRadiometer (MISR), multiple resolution tree (MRT).

I. Introduction

THE fraction of absorbed photosynthetically active radiation (FAPAR) is the fraction of incoming solar radiation absorbed by plants in the 400–700 nm spectral range [1], [2]. It is one of the 50 essential climate variables recognized

X. Tao is with the Department of Geography, The State University of New York, Buffalo, NY 14261 USA (e-mail: xintao@buffalo.edu).

S. Liang, D. Wang, and C. Huang are with the Department of Geographical Sciences, University of Maryland, College Park, MD 20742 USA.

T. He is with the Department of Geographical Sciences, University of Maryland, College Park, MD 20742 USA, and also with the School of Remote Sensing and Information Engineering, Wuhan University, Wuhan 430079, China.

by the UN Global Climate Observing System [3], and is a critical input parameter in biogeophysical and biogeochemical processes described in many climate and ecological models, e.g., community land model, community earth system model, and crop growth models [4]–[7]. FAPAR can be derived from field measurements at the point scale, but the monitoring network of *in situ* measurements is insufficient for global coverage. Satellite sensors efficiently acquire land surface information at regional and global scales, providing new opportunities for monitoring biophysical parameters [1].

An accuracy of 10% or 0.05 in FAPAR is considered acceptable in agronomical and other applications [3]. Some FAPAR products, such as those derived from Moderate Resolution Imaging Spectroradiometer (MODIS) and Multi-angle Imaging SpectroRadiometer (MISR), have accuracies approaching 0.1 [8]–[11]. The accuracy of the MODIS Collection-5 FAPAR product has been improved from Collection-4, i.e., from 0.2 to 0.1 [8], [12]–[15]. The MISR FAPAR product has an accuracy of 0.14 over crops and forests and 0.11 over grassland and savannas [16], [17]. Currently, none of these products meet the accuracy requirement of 0.05.

New sophisticated models could be developed to improve the accuracy of FAPAR estimates, but the temporal and spatial coverages of FAPAR from a single sensor are often limited by the availability of clear view observations [18]–[21]. For example, Tao *et al.* [19] estimated FAPAR from Landsat with detailed spatial distribution information but estimates were limited by the few available clear images due to the long revisit time of Landsat. An alternative is to integrate multiple data products with different characteristics and accuracies. Data fusion could overcome the problems of a single satellite product, such as missing data when clouds contaminate the scene or when instruments malfunction. It combines the advantages of different data sources, and the fusion results provide continuous spatial and temporal coverages. The uncertainty in integrated data is expected to be lower than the uncertainties in individual estimates [22].

Various data fusion methods have been developed, such as optimal interpolation (OI), empirical orthogonal function (EOF), hierarchical Bayesian model, Markov random field method, and multiple resolution tree (MRT) [23]–[27]. OI estimates the observation-to-background error variance for the noise. The method is called "optimal" because it yields

TABLE I
LIST OF THE AMERIFLUX EXPERIMENTAL SITES USED IN THIS PAPER

Site	State, Country	Latitude (°)	Longitude (°)	Land Cover
Mead Irrigated	Nebraska, US	41.1651	−96.4766	crops
Mead Irrigated Rotation	Nebraska, US	41.1649	−96.4701	crops
Mead Rainfed	Nebraska, US	41.1797	−96.4396	crops
Bartlett	New Hampshire, US	44.0646	−71.2881	deciduous broadleaf forests

a linear estimate with the least expected error when the estimated noise accurately reflects the level of actual noise in the data [28]. The disadvantage of OI is that it cannot handle large volumes of data well. It requires the inversion of the covariance matrix to consider the contributions from adjacent spatio–temporal observations, which can be very time-consuming when applied over large areas. As an alternative to geostatistical methods, methods based on EOFs have been extensively used within the geosciences. However, most existing EOF methods do not address the issues of large data sets and incompatible temporal resolutions across multiple data sets [27]. Hierarchical Bayesian models have also gained considerable traction, in part because of the advances made in overcoming computational difficulties in implementing the procedure. However, this method tends to yield wide credible intervals, which may result in ambiguity in the choice of priors, and can be computationally cumbersome [29].

Another commonly used method for image analysis is the Markov random field method, which provides a rich structure for multidimensional modeling; however, it is computationally intensive. Chou *et al.* [30] and Fieguth *et al.* [31] introduced a recursive estimator consisting of a multiscale Kalman filter and smoother over a Markov tree data structure that accommodates multiple observations with differing resolutions. At each node in the tree, the MRT method optimally blends the available observations with respect to the least mean squared error according to the Kalman gain and error characteristics of each sensor type [32]. The original MRT fills the void regions with the nearest estimated values from a coarser scale, resulting in a blocky effect. In this paper, an overlapping MRT method is utilized to interpolate values from a coarser scale to reduce the blocky effect.

Although some of these data fusion algorithms have been applied to remote sensing data, they have not been applied to integrate FAPAR products. This paper focuses on applying a data fusion method to FAPAR estimation at both the temporal and spatial domains. The aim is to improve FAPAR estimates to achieve spatial and temporal continuities with higher accuracies. The green FAPAR under both direct and diffuse radiation is considered in this paper, and the estimates are validated with *in situ* green and total FAPAR measurements [17], [19].

II. DATA

The data used in this paper include *in situ* measured FAPAR and FAPAR estimates from satellite surface reflectance data. The *in situ* measured FAPAR from four AmeriFlux sites, including one forest site and three crop sites, is collected to validate FAPAR estimates and integrations [33], [48]. We select surface reflectance data at different resolutions to estimate FAPAR, which serve as inputs in the MRT.

A. In Situ Measured FAPAR

The AmeriFlux sites can be used for temporal validation of FAPAR estimates and integrations, due to their continuous FAPAR measurements. The geolocation and land cover information of the AmeriFlux sites are listed in Table I.

Four components are measured to compute FAPAR at AmeriFlux sites, including incoming and outgoing solar flux, and the flux from and to the ground. Incoming (outgoing) solar flux is measured with Li-Cor point quantum sensors aimed upward (downward), and placed approximately 6 m above the ground. Flux transmitted through the canopy to the ground is measured with Li-Cor line quantum sensors placed approximately 2 cm above the ground, pointing upward. Flux reflected by the ground is measured with Li-Cor line quantum sensors placed approximately 12 cm above the ground, pointing downward [34]. FAPAR is calculated hourly as the ratio of absorbed photosynthetically active radiation and incoming solar flux. All daytime radiation values are computed by integrating the hourly measurements during a day when incoming solar flux exceeds 1 μmol/m^2/s, and daily FAPAR is then calculated. The spatial footprint of AmeriFlux sites is about 1 km^2. Total FAPAR measurements are used as the main validation data in this paper, considering its spatial and temporal continuities. Green FAPAR is calculated by multiplying total FAPAR with the ratio between green leaf area index (LAI) and total LAI, and is used as supplemental validation data.

B. Surface Reflectance Data

MISR, MODIS, Landsat Thematic Mapper (TM), and Enhanced TM Plus (ETM+) reflectance data are listed in Table II, and are used to estimate FAPAR based on the

TABLE II
CHARACTERISTICS OF SATELLITE SURFACE REFLECTANCE PRODUCTS USED IN THIS PAPER

Reflectance product	Temporal coverage	Temporal resolution	Spatial resolution	Projection
MISR (L2) [49]	Feb 24, 2000–	Equator: 9 days, Polar: 2 days	1 km	Space Oblique Mercator
MODIS (MOD09 C5) [50]	Feb 18, 2000–	8 days	500 m	Sinusoidal
TM [51]	Mar 1, 1984 –	16 days	30 m	Universal Transverse Mercator (UTM)
ETM+ [51]	Apr 15, 1999–	16 days	30 m	UTM

algorithm presented and validated in [18] and [19]. The MISR and MODIS FAPAR estimates are green FAPAR at 10:30 A.M. local time (LT), considering both direct and diffuse radiation absorbed by green elements. Similarly, Landsat FAPAR estimates correspond to the white-sky FAPAR by green elements between 9:30 and 10:00 A.M. LT. Overall, the satellite FAPAR estimates correspond to instantaneous FAPAR around 10:15 A.M. LT, considering both direct and diffuse radiation absorbed by the green components. The instantaneous FAPAR from satellite around 10:15 A.M. LT is often assumed to approximate the daily integrated FAPAR value [13], [35], [36]. FAPAR is assumed to remain relatively stable within a half an hour so that the integration of the satellite FAPAR estimates around 10:15 A.M. LT is reasonable. Spatial resolutions of satellite FAPAR estimates vary from 1000 to 30 m, and the temporal resolutions vary from 8 to 16 days.

III. METHOD

A. Overview of the MRT

Satellite FAPAR estimates are integrated using the MRT method to improve the accuracy of FAPAR at site and regional scales. The MRT is chosen because of its computational efficiency compared with other fusion methods, such as OI. MRT considers data continuity at multiple scales and generates multiscale data simultaneously. It is useful for making optimal predictions at multiple resolutions [37]. Here, we assume that the data at different spatial resolutions are autoregressive and can be organized in a tree structure (Fig. 1). The relationship between two adjacent layers in a tree is

$$y_u = A_u y_{\mathrm{pa}(u)} + w_u \tag{1}$$

where y_u is the variable used for estimating at scale u, and $y_{\mathrm{pa}(u)}$ is the variable at its parent node. w_u is a spatial stochastic process following a Gaussian normal distribution with a variance of W_u. A_u is a state conversion matrix to estimate the variable at scale u from its parent node. There is
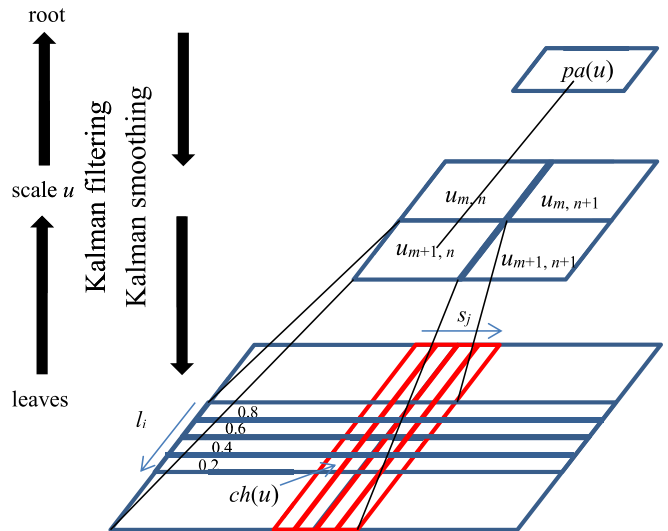

Fig. 1. Overlapping MRT algorithm. The root node is at the top and the leaves nodes are at the bottom. Coarse resolution data serve as root, and fine resolution data serve as leaves. There are two steps to implement the algorithm: Kalman filtering from leaves to root and Kalman smoothing from root to leaves. The overlapping tree structure in the Kalman smoothing process is designed to mitigate the blocky effect in the data. ch(u) denotes child node and pa(u) denotes parent node. The numbers are the weight for $u_{m,n}$ in the Kalman smoothing process.

a similar formulation that transfers from the child node ch(u) to the variable at scale u. To determine the state conversion matrix, the "change-of-support" problem has been widely discussed [37]–[39]. In this paper, y is the satellite product of FAPAR. An observation model is used to link the satellite product to the "ground truth" data

$$z_u = C_u y_u + \varepsilon_u \tag{2}$$

where z_u is the satellite product with white noise following a zero-mean Gaussian distribution with a variance of Φ_u.

C_u is the observation matrix that converts the variable of interest to satellite data. Both the variable and the satellite data are FAPAR, and hence, the observation matrix C_u is set as the identity matrix.

The MRT algorithm involves two steps: Kalman filtering from leaves to root and Kalman smoothing from root to leaves. One assumption in the MRT algorithm is that the tree structure follows a Markov chain process, which implies that the state variable is only related to its instant child and parent nodes. The first step is filtering from high to low resolution

$$\hat{y}_u = E(y_u|Z_u, Z_{\text{ch}(u)}). \tag{3}$$

The major purpose of this step is to fill the data gaps at coarser resolutions with information from high-resolution data. The second step is smoothing from low to high resolution to update the state variable with information at a coarser resolution

$$\hat{y}_u = E(y_u|Z_u, Z_{\text{pa}(u)}). \tag{4}$$

The data gaps in the high-resolution data could be filled with a conventional tree method, which would result in a blocky effect in the gaps. The overlapping tree structure is designed to apply the Kalman smoothing process to generate smooth estimates [40]. The values for the overlapping child nodes are the average of the neighboring nodes from coarser resolution. Suppose the values are interpolated from scale u to its child scale ch(u), then there will be overlapping child nodes for neighboring variables $u_{m,n}$, $u_{m+1,n}$, $u_{m,n+1}$, and $u_{m+1,n+1}$ (Fig. 1). For the child nodes located near the horizontal boundary, there will be contributions from both top and bottom variables. For example, for the horizontally overlapped child nodes of variables $u_{m,n}$ and $u_{m+1,n}$, (5) is used to determine the child node value, where l_i is the weight for $u_{m,n}$ and $(1-l_i)$ is the weight for $u_{m+1,n}$

$$\text{ch}(u)_i = l_i u_{m,n} + (1 - l_i) u_{m+1,n}. \tag{5}$$

We set the buffer zone to a size of 4, and the values of l_i to 0.8, 0.6, 0.4, and 0.2 from top to bottom, respectively (Fig. 1). Similarly, there are contributions from both left and right variables for the child nodes located near the vertical boundary, e.g., $u_{m,n}$ and $u_{m,n+1}$. Equation (6) is used to determine the child node values of variables $u_{m,n}$ and $u_{m,n+1}$, where s_j is the weight for $u_{m,n}$ and $(1 - s_j)$ is the weight for $u_{m,n+1}$

$$\text{ch}(u)_j = s_j u_{m,n} + (1 - s_j) u_{m,n+1}. \tag{6}$$

After the Kalman smoothing step, the data sets at different scales become smooth and consistent. More details of the two steps are available in [37].

B. Satellite-Based FAPAR

The surface reflectance images were converted to FAPAR by inverting a radiative transfer (RT) model, which assumes that vegetation is continuous and horizontally homogeneous. The full approach is described in [19]. The image selection, preprocessing, and FAPAR estimation steps are described in detail as follows.

We selected MISR, MODIS, and Landsat scenes around the four AmeriFlux sites on close imaging dates and with high image qualities. The image qualities are strictly controlled
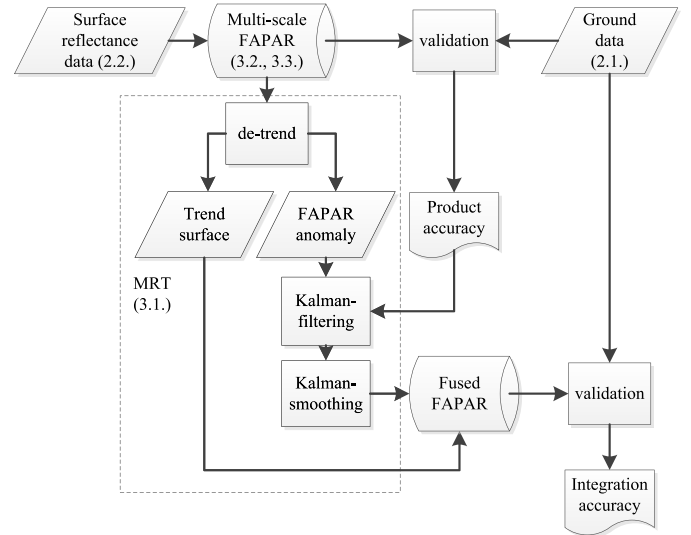

Fig. 2. Flowchart for implementing overlapping MRT algorithm. The numbers denote the sections where the corresponding data or methods are described.

so that the scenes have little or no cloud contamination. The Landsat reflectance data were atmospherically corrected using the Landsat ecosystem disturbance adaptive processing system (LEDAPS) preprocessing code [41]. Missing scan lines in the ETM+ image were filled with values from the nearest pixels.

FAPAR estimates should have the same definition and hierarchical spatial resolutions before integration [26]. In this paper, we chose to estimate FAPAR based on the same algorithm instead of using the MISR and MODIS official products for two reasons. First, there are differences in the official MISR and MODIS product definitions regarding the inclusion or exclusion of diffuse radiation [17]. The conversion to a common definition would bring some uncertainty. Second, the spatial resolutions of the MISR and MODIS FAPAR products are 1.1 and 1 km, respectively, which renders the generation of multiscale images more difficult or the corresponding statistical analysis much more complex [37], [42]. Therefore, the MISR and MODIS FAPAR estimates from the same algorithm facilitate integration in terms of consistent product definition and hierarchical spatial resolutions.

The MISR, MODIS, and Landsat images were classified into evergreen forest, deciduous forest, urban, grass, crops, barren soil, and water body. The classified images and surface reflectance images were combined to estimate vegetation FAPAR values using the model in [19]. The FAPAR estimation model is based on RT for a horizontally homogeneous continuous canopy. The spatially explicit parameterization of leaf-scattering and soil background reflectance is derived from a 13-year MODIS albedo database. The LAI input is estimated using a hybrid geometric optical-RT model suitable for both continuous and discrete vegetation canopies. The output of the model is green FAPAR, considering both direct and diffuse radiation. The general uncertainty is 0.1 when validating with total FAPAR measurements and 0.08 when validating with green FAPAR measurements, although the specific uncertainty changes at different sites. More details of the FAPAR model are available in [19].
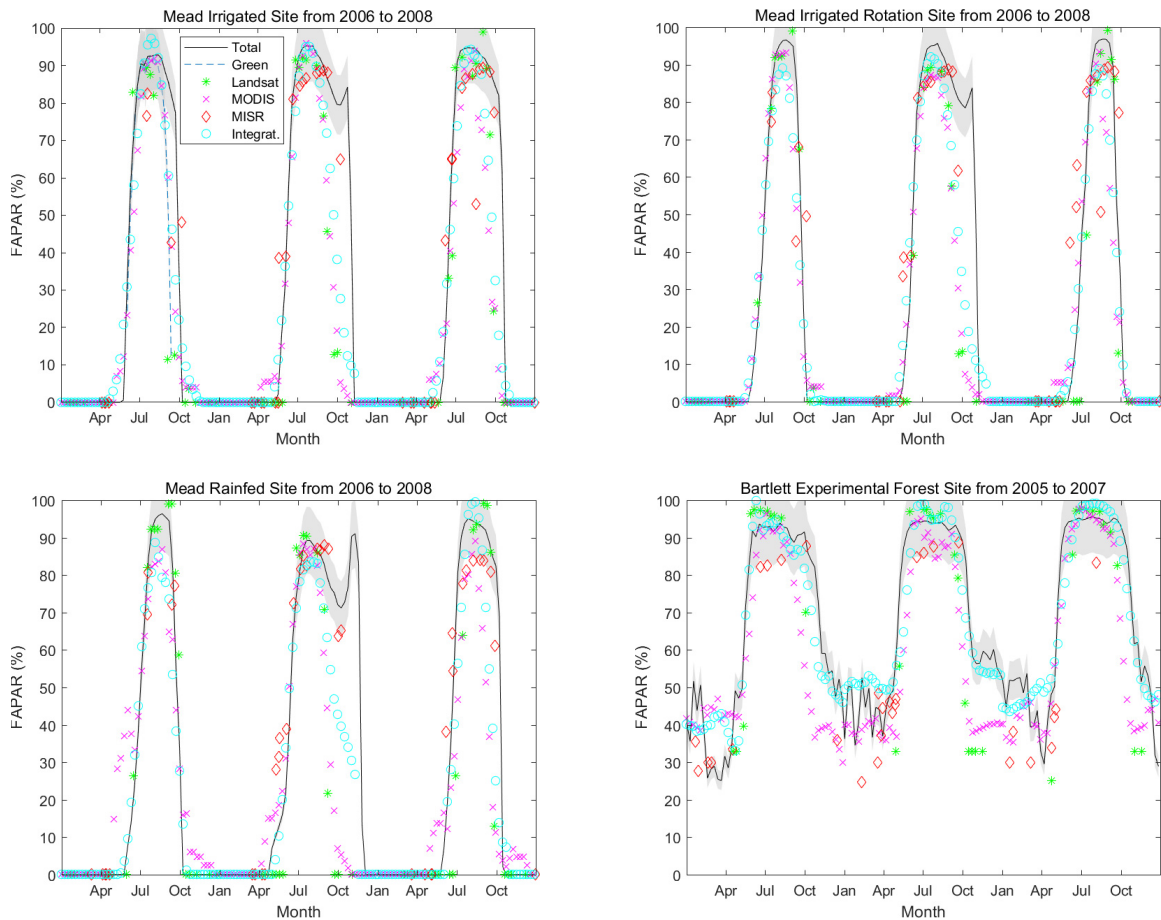
Fig. 3. Time series of *in situ* FAPAR measurements and satellite FAPAR estimates at four AmeriFlux sites. Green FAPAR measurements are depicted in blue dashed line in the first panel, and total FAPAR measurements are depicted in black line in all panels. The shaded area is the 10% accuracy requirement. The Landsat, MODIS, MISR FAPAR estimates, and FAPAR integrations are depicted in asterisks, crosses, diamonds, and circles, respectively.

C. Application of MRT to Integrate FAPAR

The MISR data were resampled to a spatial resolution of 960 m, and the MODIS 500- and 250-m data were resampled to 480 and 240 m, respectively, to construct a multiscale tree-structured model. In this case, one 960-m pixel corresponds to 2×2 480-, 4×4 240-, and 32×32 30-m pixels. The FAPAR estimates in this paper have the same definition and hierarchical spatial resolutions, so they can be directly used for integration.

The FAPAR estimates are first validated with *in situ* measurements to evaluate their accuracy. Because the retrieval algorithm is nonlinear, the different spatial scales between the FAPAR product pixels and *in situ* measurements induce an FAPAR scaling effect over heterogeneous surfaces [43], [44]. Therefore, validation results at more homogeneous sites are expected to have better FAPAR accuracy. We evaluate the heterogeneity around the validation sites by calculating their homogeneity index [17], which is calculated as the standard deviation divided by the mean of the simple ratio of the Landsat data in the 1×1 km extent around the sites. Because the distance between Mead Irrigated and Mead Irrigated rotation sites is less than 1 km, they are combined for this analysis. The impact of site heterogeneity on the accuracy of FAPAR is explored.

A flowchart that implements the overlapping MRT algorithm on multiscale FAPAR data is shown in Fig. 2. The surface reflectance data are used to estimate FAPAR based on the algorithm presented and validated in [18] and [19]. The multiscale FAPAR products are validated with *in situ* data for accuracy. A zero-mean variable is assumed in the MRT spatial process, thus the data sets are then detrended. Based on the detrended data sets, the variance W_u for child nodes linked to the same node can be calculated. For the observational error ε_u of the leaves node, the variance Φ_u can be estimated from the standard deviation of the relative difference between the fine resolution data and "ground truth." For the observational error of the nodes at all other scales, we use the standard deviation of the relative difference between the nodes and aggregated values from their child nodes. The multiscale FAPAR anomaly data are then used for integration using the MRT algorithm in two steps: Kalman filtering from high-resolution to low-resolution data and Kalman smoothing from low-resolution to high-resolution data. The updated spatial residual is added back to the trend surface to obtain the integrated product at multiple scales. Finally, the integrated product is validated with *in situ* measurements to obtain the integration accuracy. The validation statistics include bias, the mean of the deviations from the reference data, R^2 (coefficient of determination), and root-mean-square error (RMSE).
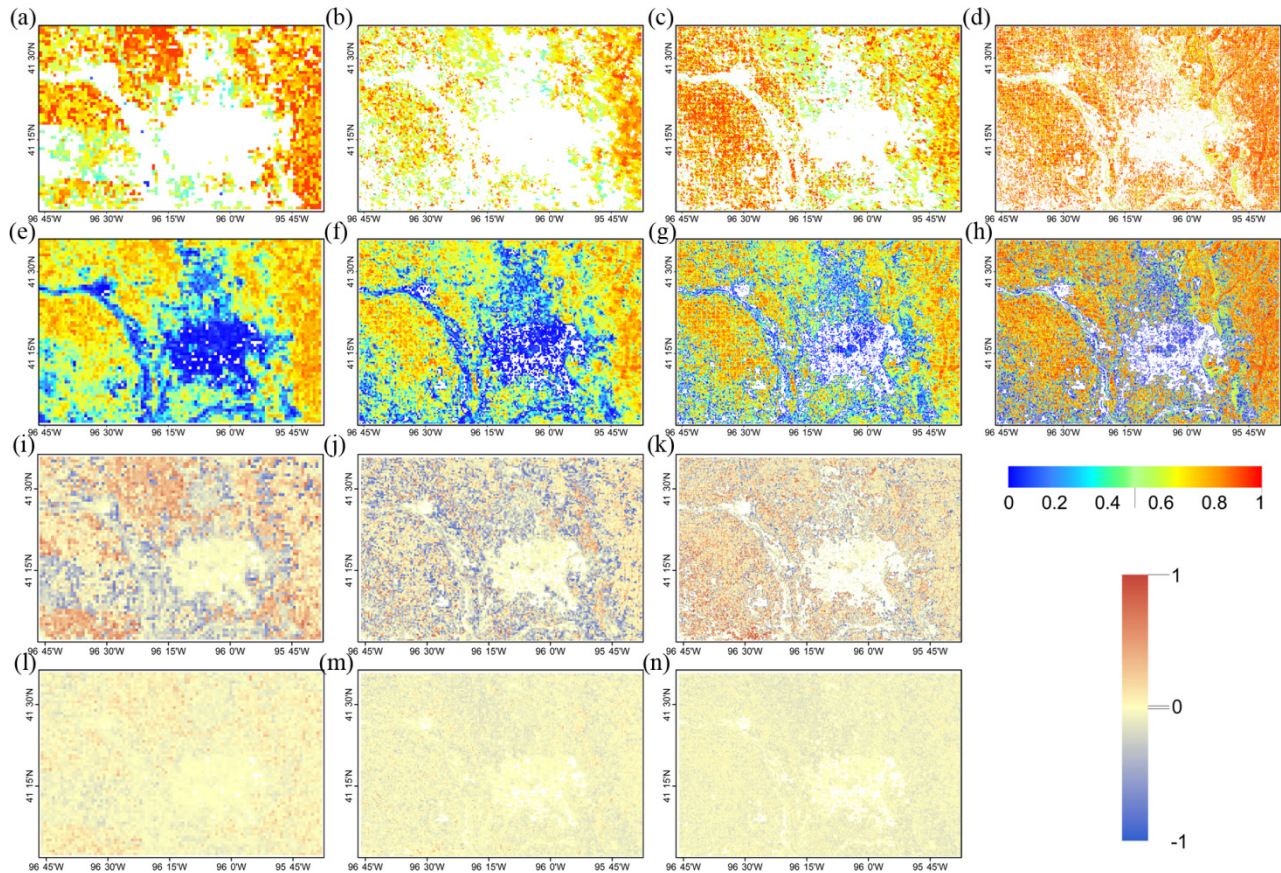
Fig. 4. FAPAR maps derived from the MISR, MODIS, and TM scenes in Case 1. (a)–(d) MISR, MODIS 480 m, MODIS 240 m, and TM FAPAR estimates before fusion are shown. (e)–(h) FAPAR after fusion is shown. The lighter areas in the map refer to nonvegetation or sparse vegetation with FAPAR values smaller than 0.01. (i)–(k) Differences of the MISR, MODIS 480 m, and MODIS 240 m FAPAR to the TM FAPAR before fusion are shown. (l)–(n) Differences after fusion are shown.

TABLE III

SPATIAL COVERAGE AND IMAGING DATE INFORMATION OF THE MODIS, MISR, AND LANDSAT DATA USED IN THE TWO REGIONAL CASES

Case	MODIS tile	MISR orbit	Landsat orbit	MODIS date	MISR date	Landsat date
1	H10V04	P27B58	P28R31	Aug 5–12, 2006	Aug 4, 2006	Aug 3, 2006
2	H12V04	P12B55	P12R29	Aug 5–12, 2005	Aug 8, 2005	Aug 8, 2005

The region in Case 1 covers three sites: Mead Irrigated, Mead Irrigated Rotation, and Mead Rainfed. The region in Cases 2 covers Bartlett site. The "H" and "V" of MODIS tile means horizontal and vertical, respectively. The "P" and "B" of MISR orbit means path and block, respectively. The "P" and "R" of Landsat orbit means path and row, respectively.

FAPAR estimates were integrated at both site and regional scales. The MRT was applied at the site scale for three consecutive years for the MISR, MODIS, and Landsat data. To make the temporal values continuous, we interpolated the satellite estimates of FAPAR at the temporal scale before integration. The temporal resolution was set to eight days so that there were 138 records of satellite FAPAR estimates in the three-year period. Table III lists the images used for the application of MRT at the regional scale. Two study regions covering the four AmeriFlux sites are selected. The imaging dates of the products differed within four days. The vegetation likely remained relatively stable within this short period and therefore, the integration of FAPAR from these different sensors is reliable. We have chosen the best quality images, but some gaps may still exist in the MISR scene because of missing values in the surface reflectance data. This is due to the strict data control on MISR surface reflectance products, including radiance angle-to-angle smoothness and image angle-to-angle correlation tests; thus, there may be large gaps in the MISR level 2 surface reflectance product [16].

IV. RESULTS

A. Site-Scale Validation

The three FAPAR estimates have similar seasonality profiles and magnitudes (Fig. 3). The FAPAR at the Mead Irrigated, Mead Irrigated Rotation, and Mead Rainfed sites reaches zero before early April and after mid-November, which is a result of crop harvesting at those locations. The biases in the MISR,

TABLE IV
STATISTICAL ANALYSIS OF COMPARISONS BETWEEN *In Situ* AND SATELLITE-BASED FAPAR ESTIMATES
OR INTEGRATIONS AT THE FOUR AMERIFLUX SITES DURING 2005–2008

Site	Product	RMSE	Bias	R^2
Mead Irrigated	MISR	0.132	−0.012	0.889
	MODIS	0.139	−0.083	0.773
	Landsat	0.224	−0.087	0.692
	Integration	0.131	−0.053	0.863
Mead Irrigated Rotation	MISR	0.181	0.034	0.774
	MODIS	0.141	−0.051	0.809
	Landsat	0.170	−0.053	0.823
	Integration	0.103	−0.039	0.901
Mead Rainfed	MISR	0.106	0.012	0.918
	MODIS	0.107	−0.069	0.632
	Landsat	0.217	−0.053	0.731
	Integration	0.124	−0.061	0.855
Bartlett	MISR	0.085	−0.083	0.898
	MODIS	0.124	−0.089	0.709
	Landsat	0.133	−0.078	0.790
	Integration	0.076	−0.005	0.877

MODIS, and Landsat FAPAR estimates are within 0.01 overall (Table IV). The MISR FAPAR has the highest accuracy at two crop sites and the forest site. The MODIS and the MISR FAPAR agree better with the *in situ* measurements at two crop sites and the forest site with respect to the magnitude than the Landsat FAPAR. The MODIS FAPAR has the lowest mean error at the Mead Irrigated Rotation site. The validation accuracy of FAPAR estimates improves from an average of 0.165 to 0.122, when using green FAPAR measurements as validation data.

The comparisons of the time-series curves of the integrated FAPAR and *in situ* measurements at the four sites are shown in Fig. 3. The time-series curves demonstrate crop or forest seasonality profiles and are smooth over a certain period of time. The RMSE reduces to an average of 0.109 and standard deviation of 0.024 for all four sites. For comparison, the average RMSE are 0.126, 0.128, and 0.186, and the standard deviations are 0.041, 0.016, and 0.043 for the MISR, MODIS, and Landsat FAPAR, respectively. The biases reduce to an average of −0.039, and the R^2 improves to around 0.874 for the four sites (Table IV). The integrated FAPAR has higher accuracy than that of the Landsat FAPAR estimates at the four sites. The integrated FAPAR has better accuracy than that of the MISR and MODIS FAPAR estimates at three sites, and its accuracy is comparable with that of the MISR and MODIS FAPAR estimates at the Mead Rainfed site.

Analysis of the spatial scaling effect on FAPAR estimates reveals that FAPAR accuracy tends to be higher in more homogeneous sites with a lower homogeneity index value. We evaluated the site homogeneity during the vegetation growing season and other seasons using Landsat images at 30-m high resolution [17]. The values for the Mead Irrigated region are 0.586 and 0.573 during the vegetation growing season and other seasons, respectively; the values for the Mead Rainfed region are 0.747 and 0.381, and the values for the Barlett region are 0.162 and 0.147, respectively. The average homogeneity indices of the two Mead regions are very close, but the homogeneity index of the Mead Irrigated region remains relatively stable.

B. Application of MRT at the Regional Scale

The FAPAR estimates are consistent across different scales in the MISR, MODIS, TM, and ETM+ images for the two cases [Figs. 4(a)–(d) and 5(a)–(d), respectively]. The values have similar distribution patterns across scales, in which the highest values are observed in evergreen forests, followed by deciduous forests and crops. Rivers and central urban areas have FAPAR estimates close to zero.

The MRT method fills the gaps in the original FAPAR estimates in the MISR data, as shown in Figs. 4(e)–(h) and 5(e)–(h) for Cases 1 and 2, respectively. Therefore, image quality is greatly improved in terms of spatial
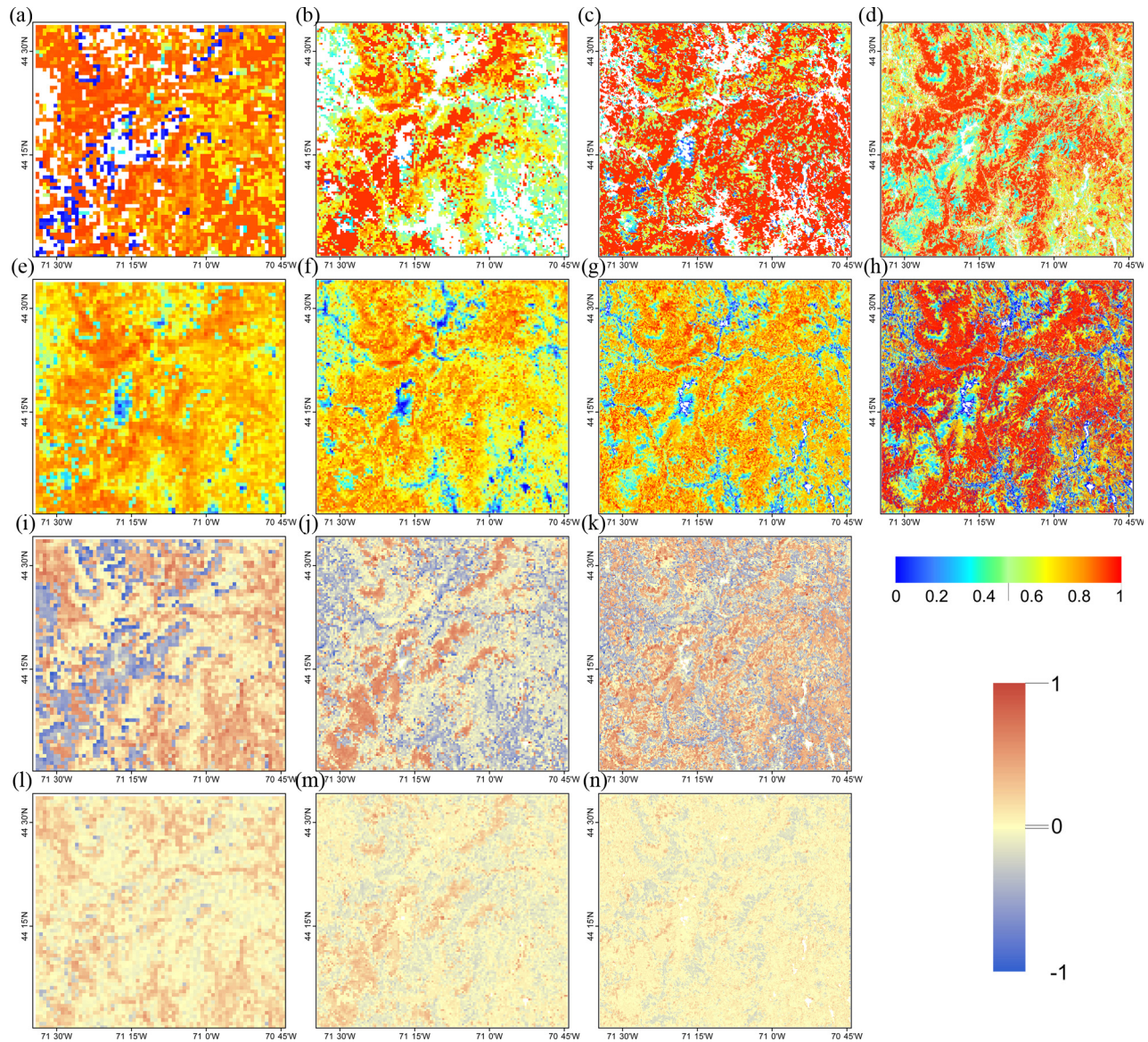
Fig. 5. FAPAR maps derived from the MISR, MODIS, and ETM+ scenes in Case 2. (a)–(d) MISR, MODIS 480 m, MODIS 240 m, and ETM+ FAPAR estimates before fusion are shown. (e)–(h) FAPAR after fusion is shown. The lighter areas in the map refer to nonvegetation or sparse vegetation with FAPAR values smaller than 0.01. (i)–(k) Differences of the MISR, MODIS 480 m, and MODIS 240 m FAPAR to the ETM+ FAPAR before fusion are shown. (l)–(n) Differences after fusion are shown.

continuity. The FAPAR distributions become more homogeneous and continuous after data fusion, which is desirable in terms of continuity among multiple-scale data. Some pixels with low values of FAPAR, less than 0.1, exist along the boundary between the vegetation and nonvegetation regions in the map after applying MRT. They are caused by the sparse vegetation observed near the river or urban area at a higher resolution. The differences become much smaller after applying the MRT method across scales for the two cases [Figs. 4(i)–(n) and 5(i)–(n), respectively].

The frequency histograms show that the standard deviation of the regional mean among the scales decreases from 0.04 to 0.03, indicating that FAPAR values agree better across scales after fusion for the two cases [Fig. 6(a) and (b) and (c) and (d), respectively]. More vegetation pixels were detected in coarse resolution images

after fusion due to integration of the high-resolution Landsat data into the coarse resolution images. The improvements are even greater when there are gaps in the original FAPAR estimates. Generally, the differences between scales in FAPAR become sufficiently small (<0.05) in both regions after fusion. Therefore, the FAPAR distributions at coarse resolutions, 960, 480, and 240 m, are closer to the distribution at the finest resolutions after data fusion.

V. DISCUSSION

This paper presents a method to integrate multiple FAPAR products at different spatial resolutions. The FAPAR integrations were validated over four validation sites, and the method was applied in two regions. The results show that the integrated FAPAR values have comparable and often improved accuracy over individual FAPAR estimates. The integrated FAPAR has
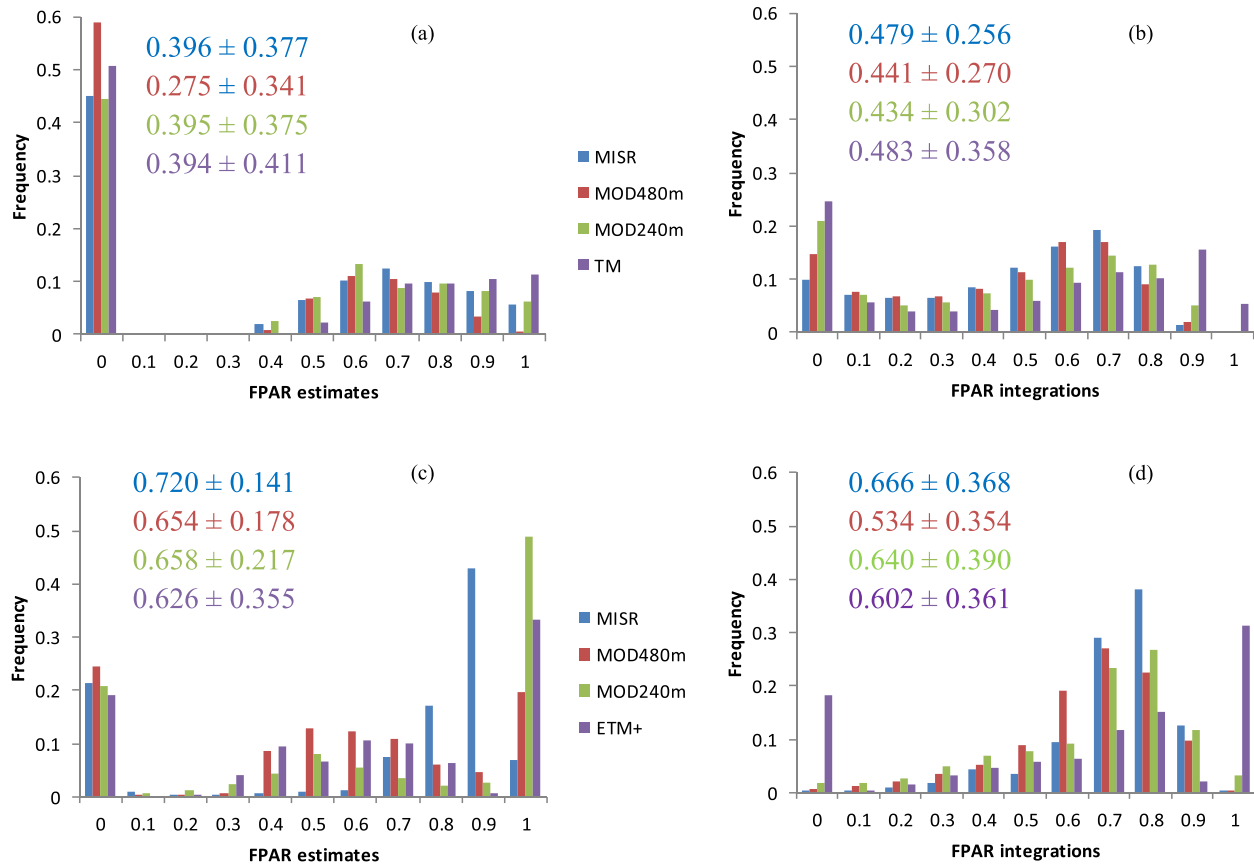
Fig. 6. FAPAR frequency histograms of the MISR, MODIS, and TM scenes in Case 1. (a) Before fusion. (b) After fusion. The frequency histograms of the MISR, MODIS, and ETM+ scenes in Case 2. (c) Before fusion. (d) After fusion. The numbers are the regional mean and standard deviation.

a reduced uncertainty, ∼0.109 when compared with some existing FAPAR products, such as MODIS, ∼0.154 and GEOV1, ∼0.113, at the validation sites [17]. The algorithm is readily available for application in regions where multiple FAPAR products are available. The existing global satellite-based FAPAR products have coarse spatial resolution, and for applications that require higher spatial resolution, such as crop growth monitoring and precision agriculture, the overlapping MRT can be used to improve data resolution, continuity, and accuracy.

The integrated FAPAR in this paper is different from some existing FAPAR products regarding definition, data requirement, and algorithm. For example, the MODIS FAPAR product is the total FAPAR at 10:30 A.M. LT, considering direct radiation absorbed by the whole canopy. The GEOV1 FAPAR product corresponds to the instantaneous black-sky FAPAR by green components around 10:15 A.M. LT. The integrated FAPAR in this paper is green FAPAR around 10:15 A.M. LT, considering both direct and diffuse radiation absorbed by green elements. In terms of data requirements and processing algorithm, the MODIS FAPAR product uses the lookup table method built on the 3-D stochastic RT model for different biomes from MODIS reflectance data [11]. GEOV1 applies a neural network to relate the fused products to the top of canopy SPOT/VEGETATION reflectance [8]. This paper applies MRT to fuse MODIS, MISR, and Landsat FAPAR

products estimated from corresponding surface reflectance data at multiple scales. Overall, most current FAPAR products do not consider absorption by diffuse radiation, and no official green FAPAR product including both direct and diffuse radiation is available [17]. Therefore, this paper serves as a good complement to the current FAPAR products. Moreover, it actively integrates high-resolution Landsat FAPAR products to provide unprecedented continuous FAPAR values at 30-m scale.

In the implementation of the method, observational errors were obtained separately for forest and crops because satellite-based FAPAR estimates perform differently across different land covers. The observational error for the AmeriFlux sites was obtained temporally considering the continuous measurements, whereas the observational error for satellite products could also be obtained spatially in a large region with a sufficient number of validation sites.

Individual FAPAR estimates and the integrated FAPAR perform better during the middle of the growing season than the beginning and end of the growing seasons. Some underestimates are generated in the latter half of the year, and specifically at the end of the growing season. The discrepancy between FAPAR estimates and *in situ* measurements at the beginning and end of the growing seasons can be attributed to two causes. One is the time difference between the MODIS and Landsat FAPAR data imaging and *in situ* mea-

surements. The temporal resolutions of MODIS and Landsat are 8 or 16 days, which may not overlap perfectly with *in situ* measurements. Therefore, the resulting FAPAR difference between satellite products and *in situ* measurements is large at the beginning and end of the vegetation growing seasons when the vegetation changes quickly. However, the time-shift issue is not a serious issue during the middle of the vegetation growing season when the vegetation remains relatively stable. Another reason for the discrepancy is the senescence and leaves turning yellow and the absorption of nonphotosynthesizing woody stems [17], [45], [46]. This results in the difference between green FAPAR and *in situ* total FAPAR measurements which includes the absorptions of both leaves and stems. This paper focusing on generating integrated FAPAR to improve the data accuracy and increasing the spatial and temporal continuities of the data. Both of the integrated FAPAR and the individual FAPAR estimates are green FAPAR. However, both green FAPAR and total FAPAR are used for validation, considering the limited number of *in situ* measured FAPAR data.

Regarding the impact of site heterogeneity on FAPAR accuracy, the vegetation in the Barlett region is more homogeneous than that in the two Mead regions; therefore, FAPAR is expected to have higher validation accuracy and lower RMSE in the former than in the latter two regions (Table IV). The averages of the homogeneity index of the two Mead regions are very close, but the homogeneity index of the Mead Irrigated region remains relatively stable. Therefore, higher validation accuracy is expected in the Mead Irrigated region than in the Mead Rainfed region. The difference between the Mead Irrigated and Mead Irrigated Rotation sites could be explained by the different crop types.

In the regional-scale fusion experiments, the FAPAR distributions before the fusion vary significantly across scales. This could be a result of the differences between the surface reflectance data arising from the differences in satellite overpass time, calibration, cloud masks, and atmospheric correction processes [47]. The differences in the FAPAR distributions are especially large when there are missing values in the images at some scales. However, the differences in FAPAR values for vegetation pixels across scales are smaller than as demonstrated in the frequency histograms in Fig. 6, which show the FAPAR distributions in the whole image, regardless of the pixel classified as vegetation. The histograms agree better across scales if the distributions of FAPAR for only vegetation pixels are displayed (see histograms shown in [19, p. 554]).

Compared with a conventional MRT method, overlapping MRT generates smooth estimations in the Kalman smoothing process. The improvement is especially significant when there are data gaps in the original high-resolution data before Kalman smoothing. The gaps were filled with values from two or four of the neighboring parent nodes instead of just one parent node. The results were more reliable and the maps were smoother than those of the conventional tree method. Due to the long satellite revisit time, such as for Landsat, there are few clear images available. The overlapping MRT method provides a mechanism for generating spatially continuous data, especially in the gaps and in high-resolution maps. With

increased data availability from some new satellites, such as Sentinel-2, the integration with these new data may help to further improve data continuity. Additionally, because more details are available in higher resolution images, the results at the finer scale are considered close to the truth. Therefore, FAPAR distributions at coarse scales are improved after data fusion in terms of image quality and accuracy as well. Further improvements on FAPAR should focus on improving the accuracy of individual FAPAR products and increasing the temporal resolution of individual products to enhance temporal matching.

VI. CONCLUSION

This paper integrated satellite FAPAR values using the MRT data fusion scheme at site and regional scales. The integrated FAPAR is a green FAPAR that considers both direct and diffuse radiation, as a complement to current FAPAR products. The overlapping MRT used in this paper improves FAPAR data accuracy, resolution, and continuity. It actively integrates high-resolution Landsat FAPAR products to provide unprecedented continuous FAPAR values at the 30-m scale, which can facilitate applications requiring higher spatial resolution, such as crop growth monitoring and precision agriculture. The integrated FAPAR reduced the biases from MODIS (-0.062) and Landsat (-0.046) to -0.019. The R^2 was improved to around 0.87, a 15% increase over the average R^2 of the individual FAPAR estimates. The integrated FAPAR values became continuous and more consistent at multiple resolutions with improved quality.

REFERENCES
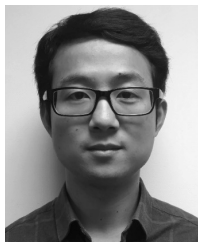
[1] S. Liang, X. Li, and J. Wang, *Advanced Remote Sensing: Terrestrial Information Extraction and Applications*. New York, NY, USA: Academic, 2012, pp. 1–799.

[2] P. J. Sellers *et al.*, "Modeling the exchanges of energy, water, and carbon between continents and the atmosphere," (in English), *Sci. Rev.*, vol. 275, no. 5299, pp. 502–509, Jan. 1997.

[3] *Systematic Observation Requirements for Satellite-Based Data Products for Climate*, document GCOS-154, GCOS, 2011, pp. 79–83.

[4] G. B. Bonan *et al.*, "The land surface climatology of the community land model coupled to the NCAR community climate model," *J. Climate*, vol. 15, no. 22, pp. 3123–3149, Nov. 2002.

[5] T. Kaminski *et al.*, "Consistent assimilation of MERIS FAPAR and atmospheric CO_2 into a terrestrial vegetation model and interactive mission benefit analysis," (in English), *Biogeosciences*, vol. 9, no. 8, pp. 3173–3184, 2012.

[6] F. Maselli, M. Chiesi, L. Fibbi, and M. Moriondo, "Integration of remote sensing and ecosystem modelling techniques to estimate forest net carbon uptake," (in English), *Int. J. Remote Sens.*, vol. 29, no. 8, pp. 2437–2443, 2008.

[7] Y. Tian *et al.*, "Comparison of seasonal and spatial variations of leaf area index and fraction of absorbed photosynthetically active radiation from Moderate Resolution Imaging Spectroradiometer (MODIS) and common land model," (in English), *J. Geophys. Res.-Atmos.*, vol. 109, no. D1, Jan. 2004, Art. no. D01103.

[8] F. Baret *et al.*, "GEOV1: *LAI* and *FAPAR* essential climate variables and *FCOVER* global time series capitalizing over existing products. Part1: Principles of development and production," *Remote Sens. Environ.*, vol. 137, pp. 299–309, Oct. 2013.

[9] N. Gobron, B. Pinty, M. Verstraete, and Y. Govaerts, "The MERIS Global Vegetation Index (MGVI): Description and preliminary application," *Int. J. Remote Sens.*, vol. 20, no. 9, pp. 1917–1927, Jun. 1999.

[10] Y. Knyazikhin, J. V. Martonchik, R. B. Myneni, D. J. Diner, and S. W. Running, "Synergistic algorithm for estimating vegetation canopy leaf area index and fraction of absorbed photosynthetically active radiation from MODIS and MISR data," (in English), *J. Geophys. Res.-Atmos.*, vol. 103, no. D24, pp. 32257–32275, Dec. 1998.

[11] R. B. Myneni *et al.*, "Global products of vegetation leaf area and fraction absorbed PAR from year one of MODIS data," (in English), *Remote Sens. Environ.*, vol. 83, nos. 1–2, pp. 214–231, Nov. 2002.

[12] F. Camacho, J. Cernicharo, R. Lacaze, F. Baret, and M. Weiss, "GEOV1: LAI, FAPAR essential climate variables and FCOVER global time series capitalizing over existing products. Part 2: Validation and intercomparison with reference products," (in English), *Remote Sens. Environ.*, vol. 137, pp. 310–329, Oct. 2013.

[13] B. Martínez, F. Camacho, A. Verger, F. J. García-Haro, and M. A. Gilabert, "Intercomparison and quality assessment of MERIS, MODIS and SEVIRI FAPAR products over the Iberian Peninsula," *Int. J. Appl. Earth Observ. Geoinf.*, vol. 21, pp. 463–476, Apr. 2013.

[14] A. McCallum *et al.*, "Comparison of four global FAPAR datasets over Northern Eurasia for the year 2000," *Remote Sens. Environ.*, vol. 114, no. 5, pp. 941–949, May 2010.

[15] C. A. Pickett-Heaps *et al.*, "Evaluation of six satellite-derived Fraction of Absorbed Photosynthetic Active Radiation (FAPAR) products across the Australian continent," (in English), *Remote Sens. Environ.*, vol. 140, pp. 241–256, Jan. 2014.

[16] J. Hu *et al.*, "Analysis of the MISR LAI/FPAR product for spatial and temporal coverage, accuracy and consistency," (in English), *Remote Sens. Environ.*, vol. 107, nos. 1–2, pp. 334–347, Mar. 2007.

[17] X. Tao, S. Liang, and D. Wang, "Assessment of five global satellite products of fraction of absorbed photosynthetically active radiation: Intercomparison and direct validation against ground-based data," *Remote Sens. Environ.*, vol. 163, pp. 270–285, Jun. 2015.

[18] X. Tao, S. Liang, and T. He, "Estimation of fraction of Absorbed Photosynthetically Active Radiation from multiple satellite data," (in English), in *Proc. IEEE Int. Geosci. Remote Sens. Symp.*, Jul. 2013, pp. 3072–3075.

[19] X. Tao, S. L. Liang, T. He, and H. Jin, "Estimation of fraction of absorbed photosynthetically active radiation from multiple satellite data: Model development and validation," (in English), *Remote Sens. Environ.*, vol. 184, pp. 539–557, Oct. 2016.

[20] Z. Xiao, S. Liang, R. Sun, J. Wang, and B. Jiang, "Estimating the fraction of absorbed photosynthetically active radiation from the MODIS data based GLASS leaf area index product," (in English), *Remote Sens. Environ.*, vol. 171, pp. 105–117, Dec. 2015.

[21] Z. Xiao, S. Liang, J. Wang, D. Xie, J. Song, and R. Fensholt, "A framework for consistent estimation of leaf area index, fraction of absorbed photosynthetically active radiation, and surface albedo from MODIS time-series data," (in English), *IEEE Trans. Geosci. Remote Sens.*, vol. 53, no. 6, pp. 3178–3197, Jun. 2015.

[22] Y. Gu, S. Bélair, J.-F. Mahfouf, and G. Deblonde, "Optimal interpolation analysis of leaf area index using MODIS data," (in English), *Remote Sens. Environ.*, vol. 104, no. 3, pp. 283–296, Oct. 2006.

[23] L. S. Gandin, *Objective Analysis of Meteorological Fields* (Israel Program for Scientific Translations). Jerusalem, Israel: Q. J. R. Meteorolog. Soc., 1965.

[24] R. Preisendorfer, *Principal Component Analysis in Meteorology and Oceanography*. New York, NY, USA: Elsevier, 1988.

[25] K. C. Chou, "A stochastic modeling approach to multiscale signal processing," Ph.D. dissertation, Dept. Elect. Eng. Comput. Sci., MIT, Cambridge, MA, USA, 1991.

[26] T. He, S. Liang, D. Wang, Y. Shuai, and Y. Yu, "Fusion of satellite land surface albedo products across scales using a multiresolution tree method in the north central United States," (in English), *IEEE Trans. Geosci. Remote Sens.*, vol. 52, no. 6, pp. 3428–3439, Jun. 2014.

[27] D. Wang and S. Liang, "Integrating MODIS and CYCLOPES leaf area index products using empirical orthogonal functions," (in English), *IEEE Trans. Geosci. Remote Sens.*, vol. 49, no. 5, pp. 1513–1519, May 2011.

[28] V. Zubko, G. G. Leptoukh, and A. Gopalan, "Study of data-merging and interpolation methods for use in an interactive online analysis system: MODIS terra and aqua daily aerosol case," *IEEE Trans. Geosci. Remote Sens.*, vol. 48, no. 12, pp. 4219–4235, Dec. 2010.

[29] P. C. Lambert, A. J. Sutton, P. R. Burton, K. R. Abrams, and D. R. Jones, "How vague is vague? A simulation study of the impact of the use of vague prior distributions in MCMC using WinBUGS," (in English), *Statist. Med.*, vol. 24, no. 15, pp. 2401–2428, Aug. 2005.

[30] K. C. Chou, A. S. Willsky, and R. Nikoukhah, "Multiscale systems, Kalman filters, and Riccati equations," (in English), *IEEE Trans. Autom. Control*, vol. 39, no. 3, pp. 479–492, Mar. 1994.

[31] P. W. Fieguth, W. C. Karl, A. S. Willsky, and C. Wunsch, "Multiresolution optimal interpolation and statistical analysis of TOPEX/POSEIDON satellite altimetry," (in English), *IEEE Trans. Geosci. Remote Sens.*, vol. 33, no. 2, pp. 280–292, Mar. 1995.

[32] H. Jhee, H.-C. Cho, H.-K. Kahng, and S. Cheung, "Multiscale quadtree model fusion with super-resolution for blocky artefact removal," *Remote Sens. Lett.*, vol. 4, no. 4, pp. 325–334, 2013.

[33] J. T. Morisette *et al.*, "Validation of global moderate-resolution LAI products: A framework proposed within the CEOS land product validation subgroup," (in English), *IEEE Trans. Geosci. Remote Sens.*, vol. 44, no. 7, pp. 1804–1817, Jul. 2006.

[34] N. P. Hanan, G. Burba, S. B. Verma, J. A. Berry, A. Suyker, and E. A. Walter-Shea, "Inversion of net ecosystem CO_2 flux measurements for estimation of canopy PAR absorption," (in English), *Global Change Biol.*, vol. 8, no. 6, pp. 563–574, Jun. 2002.

[35] T. Majasalmi, P. Stenberg, and M. Rautiainen, "Comparison of ground and satellite-based methods for estimating stand-level fPAR in a boreal forest," (in English), *Agricult. Forest Meteorol.*, vol. 232, pp. 422–432, Jan. 2017.

[36] X. Tao *et al.*, "A model for instantaneous FAPAR retrieval: Theory and validation," in *Proc. IEEE Int. Geosci. Remote Sens. Symp. (IGARSS)*, vol. 1. New York, NY, USA, Jul. 2009, pp. I-144–I-147.

[37] H.-C. Huang, N. Cressie, and J. Gabrosek, "Fast, resolution-consistent spatial prediction of global processes from satellite data," *J. Comput. Graph. Statist.*, vol. 11, no. 1, pp. 63–88, Mar. 2002.

[38] C. Plumejeaud, H. Mathian, J. Gensel, and C. Grasland, "Spatio-temporal analysis of territorial changes from a multi-scale perspective," (in English), *Int. J. Geograph. Inf. Sci.*, vol. 25, no. 10, pp. 1597–1612, Aug. 2011.

[39] C. K. Wikle, "Hierarchical models in environmental science," (in English), *Int. Statist. Rev.*, vol. 71, no. 2, pp. 181–199, Aug. 2003.

[40] W. W. Irving, P. W. Fieguth, and A. S. Willsky, "An overlapping tree approach to multiscale stochastic modeling and estimation," (in English), *IEEE Trans. Image Process.*, vol. 6, no. 11, pp. 1517–1529, Nov. 1997.

[41] J. G. Masek *et al.*, "A Landsat surface reflectance dataset for North America, 1990–2000," (in English), *IEEE Geosci. Remote Sens. Lett.*, vol. 3, no. 1, pp. 68–72, Jan. 2006.

[42] J. Zhu, C. L. S. Morgan, J. M. Norman, W. Yue, and B. Lowery, "Combined mapping of soil properties using a multi-scale tree-structured spatial model," (in English), *Geoderma*, vol. 118, nos. 3–4, pp. 321–334, Feb. 2004.

[43] X. Tao *et al.*, "Scale transformation of Leaf Area Index product retrieved from multiresolution remotely sensed data: Analysis and case studies," *Int. J. Remote Sens.*, vol. 30, no. 20, pp. 5383–5395, 2009.

[44] X. Xu, W. Fan, and X. Tao, "The spatial scaling effect of continuous canopy Leaves Area Index retrieved by remote sensing," *Sci. China D, Earth Sci.*, vol. 52, no. 3, pp. 393–401, Mar. 2009.

[45] A. Viña and A. A. Gitelson, "New developments in the remote estimation of the fraction of absorbed photosynthetically active radiation in crops," (in English), *Geophys. Res. Lett.*, vol. 32, no. 17, Sep. 2005, Art. no. L17403.

[46] B. Pinty, T. Lavergne, J.-L. Widlowski, N. Gobron, and M. M. Verstraete, "On the need to observe vegetation canopies in the near-infrared to estimate visible light absorption," (in English), *Remote Sens. Environ.*, vol. 113, no. 1, pp. 10–23, Jan. 2009.

[47] N. Gobron *et al.*, "Uncertainty estimates for the FAPAR operational products derived from MERIS—Impact of top-of-atmosphere radiance uncertainties and validation with field data," (in English), *Remote Sens. Environ.*, vol. 112, no. 4, pp. 1871–1883, Apr. 2008.

[48] *The AmeriFlux Validation Data*. Accessed: Dec. 12, 2017. [Online]. Available: http://ameriflux.lbl.gov/

[49] *The MISR Data*. Accessed: Dec. 12, 2017. [Online]. Available: http://l0dup05.larc.nasa.gov/MISR/cgi-bin/MISR/main.cgi

[50] *The MODIS Collection 5 Data*. Accessed: Dec. 12, 2017. [Online]. Available: https://ladsweb.modaps.eosdis.nasa.gov/search/

[51] *The Landsat TM and ETM+ Data*. Accessed: Dec. 12, 2017. [Online]. Available: http://espa.cr.usgs.gov/

Dongdong Wang received the B.S. degree in environmental sciences from Peking University, Beijing, China, and the Ph.D. degree in geography from the University of Maryland, College Park, MD, USA.

He is currently an Associate Research Professor with the Department of Geographical Sciences, University of Maryland. His research interests include remote sensing of surface radiation budget, integration of high-level remote sensing land products, climate change, and terrestrial ecosystem.

Xin Tao received the Ph.D. degree in geography from the University of Maryland, College Park, MD, USA.

He is currently a Clinical Assistant Professor with the Department of Geography, The State University of New York, Buffalo, NY, USA. His research interests include the estimation of biogeophysical variables from satellite data, data fusion of satellite products, and scaling effect and scale transformation of biogeophysical variables.

Tao He received the B.E. degree in photogrammetry and remote sensing from Wuhan University, Wuhan, China, in 2006, and the Ph.D. degree in geography from the University of Maryland, College Park, MD, USA, in 2012.

He is currently a Professor with the School of Remote Sensing and Information Engineering, Wuhan University, and also with the Department of Geographical Sciences, University of Maryland. His research interests include surface anisotropy and albedo modeling, data fusion of satellite products, and long-term regional and global surface radiation budget analysis.

Shunlin Liang (M'94–F'13) received the Ph.D. degree from Boston University, Boston, MA, USA.

He is currently a Professor with the Department of Geographical Sciences, University of Maryland, College Park, MD, USA. He has authored over 300 SCI indexed peer-reviewed journal papers and 32 book chapters. He has authored or edited six books and four of which were also published in Chinese, such as *Quantitative Remote Sensing of Land Surfaces* (Wiley, 2004), *Advances in Land Remote Sensing: System, Modeling, Inversion and Application* (Springer, 2008), *Advanced Remote Sensing: Terrestrial Information Extraction and Applications* (Academic Press, 2012), *Global LAnd Surface Satellite (GLASS) Products: Algorithms, Validation and Analysis* (Springer, 2013), *Land Surface Observation, Modeling, Data Assimilation* (World Scientific, 2013), and *Earth's Energy Budget* (Elsevier, 2017). His research interests include the estimation of land surface variables from satellite data, earth's energy balance, and assessment of environmental changes.

Dr. Liang was the Editor-in-Chief of the nine-volume books titled *Comprehensive Remote Sensing* (Elsevier, 2017). He was an Associate Editor of the IEEE TRANSACTIONS ON GEOSCIENCE AND REMOTE SENSING and also a guest editor of several remote sensing-related journals.

Chengquan Huang received the B.S. and M.S. degrees from Peking University, Beijing, China, and the Ph.D. degree from the University of Maryland, College Park, MD, USA.

He is a currently a Research Professor with the Department of Geographical Sciences, University of Maryland. His research interests include remote sensing of land cover and vegetation dynamics and related applications.